Synergistic PF_6^- and FSI- intercalation enables stable graphite cathode for potassium-based dual ion battery

Hong Tan [a], Dengyun Zhai [b], Feiyu Kang [b,c], Biao Zhang [a] *

[a] Department of Applied Physics, The Hong Kong Polytechnic University, Kowloon, Hong Kong, China

[b] Shenzhen Key Laboratory for Graphene-Based Materials, Shenzhen International Graduate School, Tsinghua University, Shenzhen 518055, China

[c] School of Materials Science and Engineering, Tsinghua University, Beijing 100084, China

*Corresponding author. E-mail: biao.ap.zhang@polyu.edu.hk

Abstract:

Potassium-based dual ion batteries have emerged as promising alternatives to the prevailing lithium-ion batteries due to the advantages in cost and sustainability. Single-anion intercalation into graphite takes place on the cathode side, but it usually delivers a low capacity with poor Coulombic efficiency in potassium-based systems. We demonstrate the performance could be significantly boosted through synergistic dual-anion intercalation of FSI- and PF_6^-. The presence of PF_6^- helps the formation of an effective cathode electrolyte interface to allow high anionic stability up to 5.5 V, while FSI- intercalation brings about superior rate capability and long-term cyclic stability. Concurrent intercalation of FSI- and PF_6^- is tracked by in-situ Raman spectroscopy and ex-situ XRD. It reveals the formation of stage I graphite intercalation compounds (GICs) upon charging, leading to a reversible capacity of over 100 mAh g^{-1} with an average potential of 4.65 V (vs. K^+/K). Furthermore, the graphite-potassium cell delivers an exceptional capacity of 94 mAh g^{-1} at 0.3 A g^{-1} and shows capacity retention of 96% after 250 cycles. The strategy provides a novel avenue toward stable dual-ion battery via intercalation chemistry regulation.

Keywords: graphite cathode, anion intercalation, in-situ Raman, dual ion batteries

1

1. Introduction

Developing low-cost, eco-friendly energy storage systems is critical to meeting the ever-expanding energy demand as well as dealing with environment-deterioration and sustainability issues [1,2]. In this context, dual-ion batteries (DIBs) are emerging as promising alternatives to the prevalent Li-ion batteries (LIBs) [3]. On the one hand, the adoption of natural abundant graphite as cathode reduces the cost and raises the environmental benignity by eliminating precious and toxic metals like cobalt [4]. On the other hand, the feasibility of replacing Li with other abundant elements such as K [5], Na [6,7], Al [8,9], and Zn [10] in DIBs helps address the scarcity problem of lithium and provides flexible options for different application scenarios.

Potassium-based dual-ion batteries (P-DIBs) have attracted vast research interest due to the similar redox potential of K^+/K (2.93 V vs. standard hydrogen electrode, SHE) with Li^+/Li (3.04 V vs. SHE), which predicts high working voltage and thus high energy density. Previous works on P-DIBs have demonstrated a reversible capacity of around 60-70 mAh g^{-1} using 0.8-1.0 mol L^{-1} (M) KPF_6 in carbonate electrolytes [11–13]. This performance stays unsatisfied compared to the counterparts in Li-based systems [14,15]. Fully intercalation of the anion such as PF_6^- necessitates a high charge potential approaching 5.5 V, which brings about great challenges on the electrolyte and the cell system against oxidation. The issue is normally tackled by adopting highly concentrated electrolyte such as over 3M $LiPF_6$ in Li-based DIBs [16]. The strategy is partly restricted by the limited solubility of KPF_6 (< 1 M) in carbonates for P-DIBs [17]. Consequently, intensified concentration polarization upon charging occurs, leading to insufficient anion storage within normal charge-discharge window. Besides, severe decomposition of electrolytes could take place at high voltage, which not only suppress the intercalation process but also lead to a low Coulombic efficiency of around 90%. Optimization on both the salt and solvent of electrolyte are conducted to address the challenges. Winter's group demonstrate the efficiency could be improved to over 99% by utilizing an ionic liquid

electrolyte [18]. Owing to the narrow electrochemical window, a capacity of less than 50 mAh g^{-1} is obtained. Taking advantages of the high solubility of KFSI, a concentrated electrolyte of 5 M KFSI in EC/DMC is then constructed to improve the electrolyte stability and realize effective FSI^- intercalation [19]. As a result, the P-DIBs delivers an exceptional capacity close to 100 mAh g^{-1} at a moderate current density of 50 mA g^{-1} and a decent Coulombic efficiency of over 95%.

Novel intercalation chemistry is required to realize the full anion intercalation while suppressing the devastating parasite reactions. Multi-ion strategy has been widely used in both non-aqueous and aqueous electrolytes. The presence of different cations/anions is proved effective in enhancing the diffusivity and cycling reversibility as well as the chemical stability by combining the advantages of each component [20–23]. Dual-anion intercalation is predicated to benefit the high capacity cathode in DIBs in the progress report by Tang et al [24]. The approach has yet to be realized although with such an open call. The reasons may lie in the competitive instead of cooperative intercalation behaviors when multi-anions present. Herein, we report the synergistic interaction of FSI^- and PF_6^- to realize a stable capacity of 100 mAh g^{-1} with superior rate capability. Detailed staging process upon intercalation/de-intercalation is revealed by in-situ Raman spectroscopy and ex-situ X-ray diffraction (XRD).

2. Experimental

2.1 Preparation of free-standing graphite film and electrolytes

In a typical synthesis, 0.05 g Poly vinylidene fluoride-co-hexafluoropropylene (PVDF-HFP, Sigma Aldrich. Co) was dissolved in 2.5 ml acetone (ACS grade, Anaqua Global International Inc. Ltd) in a glass bottle. Then, 0.2 g Graphite flake powder (GFP) (Guangdong Canrd New Energy Technology Co., Ltd) was added into the solution with vigorously stirring for 6h. Subsequently, the homogeneous solution was poured into a flat-bottomed watch-glass (Fig. S1). After complete volatilization of acetone, the free-standing graphite film (FGF) could be

collected. The binder does not participate in the reaction. A relatively large amount of 20wt% was used to make a mechanically stable film [25–27]. Free-standing tungsten film for LSV test was prepared in the same way except that tungsten powder was added into the acetone solution with PVDF-HFP. The above process was carried out in a fume hood.

Ethylene carbonate (EC), dimethyl carbonate (DMC) and ethyl methyl carbonate (EMC) were first mixed with a ratio of 3:2:5 by weight under vigorously stirring. Potassium bis(fluorosulfonyl)imide (KFSI, TCI (Shanghai) development Co., Ltd.) and/or potassium hexafluorophosphate (KPF$_6$, DoDoChem) were/was then added to form the targeted electrolytes. The KPF$_6$ was dried in a vacuum chamber at 80 ℃ overnight before use. The preparation of electrolytes was performed in a glove box filled with Argon.

2.2 Electrochemical measurement

Graphite discs with a diameter of 9 mm were punched from the as-prepared free-standing graphite film and were directly used as the working electrode. Each electrode has a graphite loading of around 2 mg. Swagelok cells (Fig. S2) were assembled using a potassium plate counter electrode and a piece of glass fiber separator (Whatman, GF/D) containing 80 uL electrolyte. In particular, an aluminum rod was used as the current collector on the cathode side and a carbon-coated aluminum foil with a diameter of 12 mm was placed in-between the Al rod and graphite working electrode. The assembly was processed inside a glovebox with O$_2$ and H$_2$O content below 0.5. K-K symmetric cells and K-graphite cells for temperature test were assembled within R2032 coin cell configurations. In particular, K plates with a diameter of 9 mm were used in the K-K cells. A piece of carbon-coated aluminum foil with a diameter of 20 mm is placed between the battery cover and the FGF electrode for K-graphite cells. The linear sweep voltammetry (LSV), cyclic voltammetry (CV) and electrochemistry impedance spectroscopy (EIS) measurements were performed on a SP150 (Biologic, France) workstation. Galvanostatic tests were carried out on LAND CT2001A Battery Testing systems.

2.3 Characterizations

Energy dispersive X-ray spectroscopy (EDS) was performed on a TESCAN VEGA 3 thermionic emission scanning electron microscope (SEM) system. X-ray photoelectron spectroscopy (XPS) was taken on Nexsa X-ray Photoelectron Spectrometer system (Thermo Fisher Scientific Inc.) using a monochromatic Al Kα radiation. Raman scattering was operated using a Witec-Confocal Raman system (UHTS 600 SMFC VIS) with a laser wave length of 532nm. The X-ray diffraction (XRD) patterns were collected on Rigaku Smart Lab 9kW Diffractometer using Cu-Kα radiation (λ=1.54178Å). Fourier Transform Infrared Spectroscopy (FTIR) measurement was conducted on a Bruker VERTEX 70 system. Microstructures of the K anode before and after cycling were characterized by Atomic Force Microscope (AFM) using a Bruker Icon Dimension XR system.

To perform the EDS and ex-situ XRD experiments, the cells at different charge/discharge states were dis-assembled in a glove box with Ar protection. Afterward, the graphite films were washed with DMC for several times to eliminate the remaining electrolytes. For XPS characterization, the graphite powder, instead of free-standing graphite film, was directly adopted as the working electrode to avoid the interference of PVDF-HFP. The cycled powder was also washed with DMC to prevent the influence of impurities. After that, the graphite powder was directly attached to a conductive carbon glue within a vacuum transfer chamber for the test.

3. Results and Discussion

3.1. Electrochemical stability

A ternary solvent system of ethylene carbonate (EC) - dimethyl carbonate (DMC) - ethyl methyl carbonate (EMC) (3:2:5 by weight) is chosen in the interest of combining the merit of each component. While EC guarantees the salt solubility, DMC helps lower the viscosity. EMC

takes 50% proportion as it facilitates the effective de-intercalation of anions in DIBs [28,29]. The dual-anion strategy is examined starting with the determination of the electrochemical window of single- and dual-salt electrolytes with different KFSI-KPF$_6$ molar ratios (marked as xFSI-yPF$_6$, x and y denotes the molar number). The concentration is fixed at 0.8 M with an exception of pure KPF$_6$ electrolyte, which could only reach around 0.7 M at maximum. The presence of different salts is confirmed by Raman spectra (Fig. S3) without the detection of interaction between the two salts [30]. Slightly enhanced ionic conductivities are observed for such electrolytes as the amount of KFSI increases, which indicates a value of 0.34, 0.43 and 0.66 mS·cm^{-1} for 0.7M KPF$_6$, 0.3KFSI-0.5KPF$_6$ and 0.8M KFSI, respectively (Fig. S4). To examine the electrochemical window of the various salt/solvent combinations, a tungsten (W) film was used as the cathode during the Linear sweep voltammetry (LSV) test to avoid the interference from the working electrode [19].
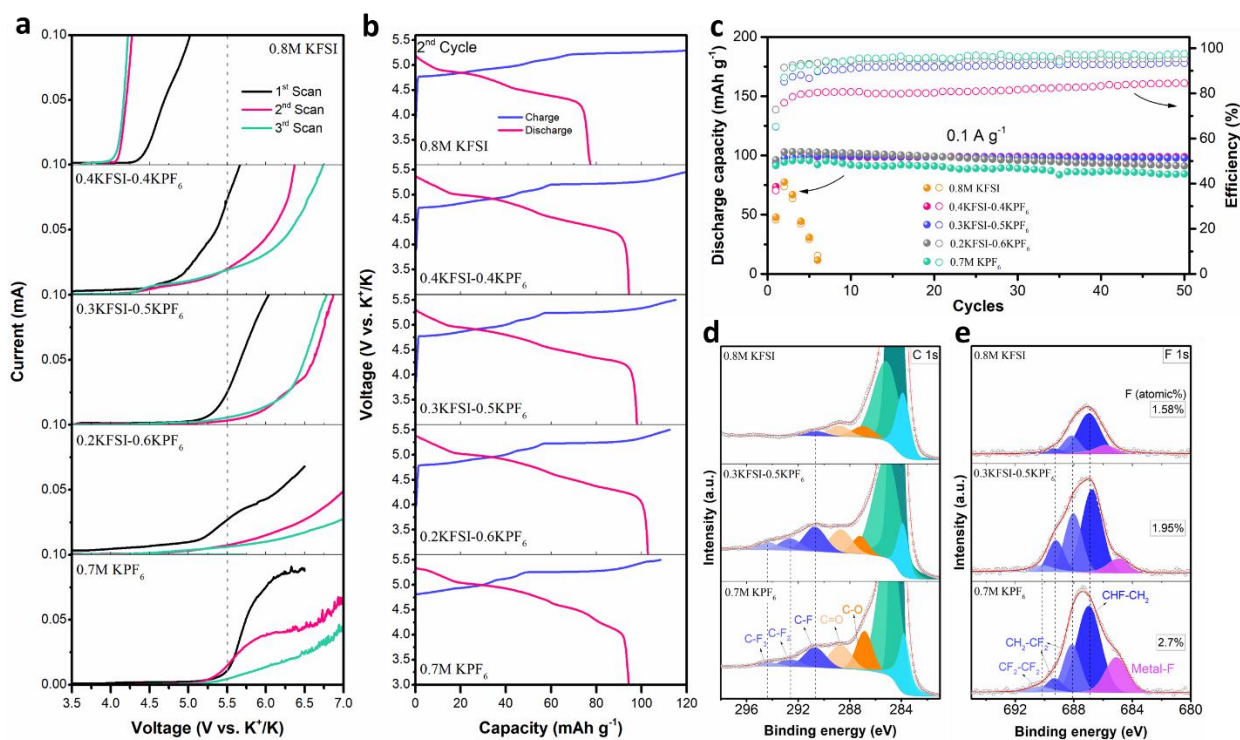

Fig. 1. (a) LSV of different electrolyte systems using tungsten plate as cathode at a scan rate of 2 mV s^{-1}, the corresponding (b) voltage profiles and (c) cycling performance using graphite as cathode. (d) C 1s

and (e) F 1s XPS surface profiles of graphite electrodes cycled with 0.8 M KFSI, 0.3KFSI-0.5KPF$_6$ and 0.7 M KPF$_6$.

As shown in **Fig. 1**a, 0.8 M KFSI electrolyte suffers from severe electrolyte deterioration below 4.5 V in the first scan and 4.0 V in the following scans. For dual-salt electrolytes, KFSI-KPF$_6$ with a salt ratio of 0.4/0.4, 0.3/0.5 and 0.2/0.6 displays primarily an oxidation voltage of 4.75 V, 5.25 V and 5.2 V, respectively. Due possibly to the formation of cathode electrolyte interface (CEI), the chemical windows for 0.3KFSI-0.5KPF$_6$ and 0.2KFSI-0.6KPF$_6$ are expanded beyond 5.5 V after the 2nd scan. Noteworthy is that the 0.7 M KPF$_6$ electrolyte initially shows an oxidation potential at around 5.5 V and also has its decomposition current suppressed in the subsequent scans. The above results suggest the necessity of incorporating KPF$_6$ salt to achieve sufficient stability of the electrolyte against oxidation at a high voltage.

Galvanostatic experiments were then carried out to test those electrolytes in P-DIBs using freestanding graphite flake film as cathode and potassium plate as anode in a Swagelok cell. A Bellcore's plastic method was used to prepare the cathode film, which consists of 80% graphite and 20% Poly vinylidene fluoride-co-hexafluoropropylene (PVDF-HFP) [31]. An aluminum foil coated with amorphous carbon was placed in-between the Al current collector and graphite to avoid corrosion on the Al rod. The configuration of the cells is presented in the supporting information. The amorphous nature of the coated carbon is characterized by XRD and Raman spectroscopy, which show negligible capacity toward anion intercalation (Fig. S5). The voltage profiles of 2nd cycle within 3.0-5.5 V under different electrolytes are shown in Fig. 1b. The cell with 0.8 M KFSI electrolyte experiences overcharging with an abnormal plateau below 5.5 V and decays rapidly within a few cycles at 0.1 A g^{-1} (Fig. 1c). Dis-assembly of the cycled cell reveals that both the Al current collector and the carbon-coated Al foil are both heavily corroded at high voltage (Fig. S6). In comparison, cells using dual-salt- and 0.7 M KPF$_6$ electrolytes possess intact charge-discharge curves. With the incorporation of 0.4 M KPF$_6$, a reversible

capacity of 95 mAh g^{-1} is obtained although the Coulombic efficiency is quite low due to the severe electrolyte decomposition. The parasitic reactions from the electrolyte could be largely suppressed with the increased amount of KPF$_6$, as demonstrated in 0.3KFSI-0.5KPF$_6$ and 0.2KFSI-0.6KPF$_6$ system, which agrees well with LSV test in Fig. 1a. Furthermore, the presence of KPF$_6$ essentially increases the reversible capacity, achieving a capacity of 103 mAh g^{-1} under the 0.2KFSI-0.6KPF$_6$. Nevertheless, full exclusion of KFSI salt in the electrolyte would also degrade the performance. The cell with single KPF$_6$ salt electrolyte delivers a mediate capacity of 94 mAh g^{-1} with obvious capacity fading in only 50 cycles (Fig. 1c). A synergistic effect in the capacity and stability is realized in the dual-salt electrolyte of 0.3KFSI-0.5KPF$_6$. Note that the capacity obtained here is almost 50% higher than the value reported previously under such a limited concentration, suggesting the essential of realizing 5.5 V charge voltage and adopting appropriate anions to allow the full intercalation, as will be discussed later.

To understand the origin of chemical stability, XPS surface analysis was carried out on the neat graphite powder cycled with both dual-ion and single-salt electrolytes. The samples were obtained by dis-assembling the batteries after three cycles in a glove box filled with ultra-pure Ar. After washing with DMC and natural drying, the samples were directly attached to the conductive carbon glue and transferred using a vacuum chamber to avoid degradation in air. As shown in Fig. 1d, the C1s spectrum of 0.8 M KFSI implies the formation of C-O, C=O as well as C-F species [22,32–34]. By contrast, an obvious enrichment of C-F species along with the appearing of C-F$_2$ and C-F$_3$ (minor) species is observed for 0.3KFSI-0.5KPF$_6$ and 0.7 M KPF$_6$. Accordingly, the F1s spectra (Fig. 1e) confirm the minor amount of CHF-CH$_2$, CH$_2$-CF$_2$ and CF$_2$-CF$_2$ species for 0.8 M KFSI [35–37], compared with 0.3KFSI-0.5KPF$_6$ and 0.7 M KPF$_6$, which is in good agreement with the results by C1s spectra. The fluorine in the as-obtained CEI comes largely from the breakdown of PF$_6^-$ at high voltage. For O1s spectrum (Fig. S7), oxygen-containing species like O-C=O, O-H and C-O are verified, suggesting that the carbonate-based

8

solvents are involved in the formation of organic species within CEI [22]. The effective formation of fluorine and oxygen abundant CEI layers are also confirmed by FTIR characterization on graphite film electrodes cycled under 0.3KFSI-0.5KPF$_6$ and 0.7 M KPF$_6$ electrolytes (Fig. S8). The formation of fluorine-abundant species has been proven beneficial in stabilizing CEI at high voltage [38], which accounts for the enhanced performance of 0.3KFSI-0.5KPF$_6$ electrolyte.

3.2 Dual-anion intercalation mechanisms

To investigate the synergistic effect of FSI$^-$ and PF$_6^-$ on the electrochemical process, cyclic voltammetry (CV) was carried out for 0.8 M KFSI, 0.3KFSI-0.5KPF$_6$ and 0.7 M KPF$_6$ electrolytes with a scan range of 3.0-5.5 V. As shown in **Fig. 2**a, both the cells under 0.8 M KFSI and 0.3KFSI-0.5KPF$_6$ have four oxidation peaks (O1, O2, O3 and O4 at 4.87, 5.00, 5.14 and 5.34~5.37 V, respectively) and two reduction peaks (R1 and R2 at 4.91 and 4.30~4.38 V, respectively) in their CV curves. For 0.7 M KPF$_6$, the O1 peak becomes less obvious and the other three oxidation peaks (O2, O3, O4) and reduction peak R1 appear at similar potentials with those of 0.8 M KFSI and 0.3KFSI-0.5KPF$_6$, whereas R2 shifts down to 4.26 V. Besides, a pair of peaks appear at very high potentials, namely the O' at around 5.45 V and R' at 5.35 V, which are in accordance with the short plateaus in the corresponding charge-discharge curves in Fig. 1b. Except for R1, R2, and R', a couple of minor peaks (R1' and other two denoted by arrows) are observable upon cathodic scan for 0.7 M KPF$_6$. All the oxidation/reduction peaks should arise from the reactions between the intercalant and graphite bulk to form various staged K-GICs, which will be discussed later. Although 0.3KFSI-0.5KPF$_6$ comprises a larger ratio of PF$_6^-$, the corresponding CV curve resembles that of 0.8 M KFSI rather than 0.7 M KPF$_6$, indicating that FSI$^-$ plays a major role in the reactions. One possible reason could be that PF$_6^-$ intercalation/de-intercalation into graphite is suppressed by FSI$^-$ due to the higher de-solvation energy of KPF$_6$ [19].

To monitor the charge intercalation process, the amount of PF_6^- and FSI^- intercalants are calculated based on the sulfur (S) and phosphorus (P) contents measured by EDS (Table S1, S2). Fig. 2b shows the evolution of the intercalants/carbon ratio at various charge/discharge depths for 0.3KFSI-0.5KPF$_6$ and 0.2KFSI-0.6KPF$_6$ electrolytes. It can be seen that FSI^- and PF_6^- are simultaneously involved in the intercalation/de-intercalation processes. For 0.3KFSI-0.5KPF$_6$, FSI^- makes predominant contribution to the overall capacity through the entire charge-discharge process although it constitutes less than half of the total salts in mole ratio. A much-balanced amount of FSI^- and PF_6^- is obtained in 0.2KFSI-0.6KPF$_6$, where FSI^- takes only slightly priority during intercalation. The intercalated amount ratio of FSI^-/PF_6^- is 3.5/1 and 1.125/1 at 5.5 V for 0.3KFSI-0.5KPF$_6$ and 0.2KFSI-0.6KPF$_6$, respectively, showing distinct intercalation behaviors. Note that the value presented only qualitatively reflects the related amount of the intercalants due to the limited probing depth and accuracy of EDS technique. Fig. 2c shows the typical mapping result of FGF electrode charged to 5.5 V with 0.3KFSI-0.5KPF$_6$. A homogeneous distribution of P and S is displayed arising from the almost evenly integrated intercalation of PF_6^- and FSI^-, where a predominant amount of S presents due to the prime FSI^- intercalation.
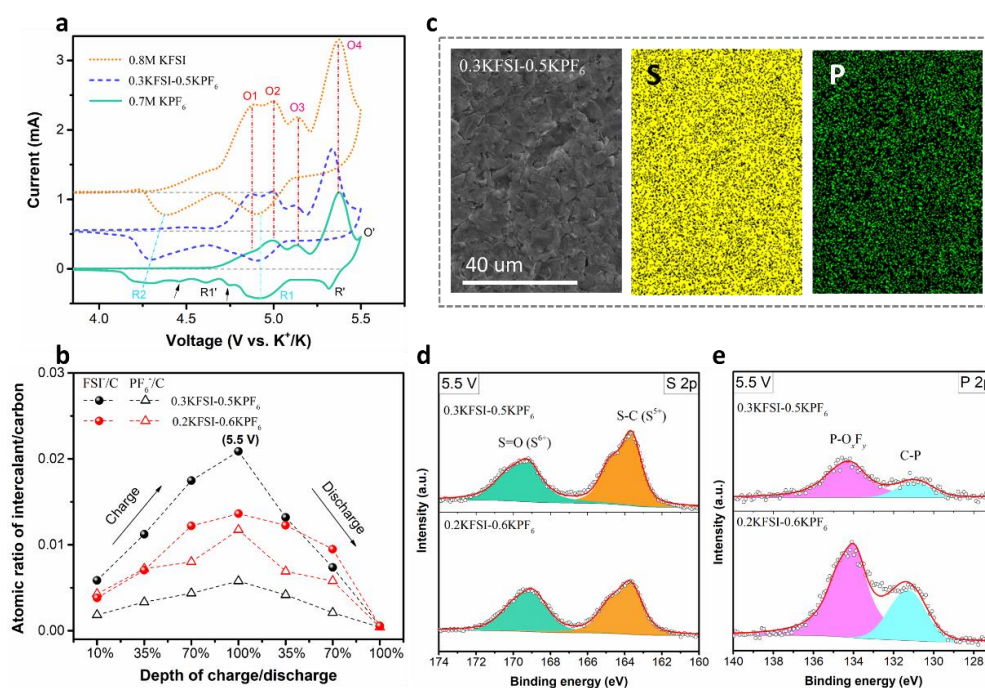
Fig. 2. (a) Cyclic voltammetry of 0.8 M KFSI, 0.3KFSI-0.5KPF$_6$ and 0.7 M KPF$_6$ at 0.5 mV s^{-1}. (b) atomic ratio of intercalants/carbon by EDS analysis of FGF electrodes at different depth of charge/discharge using 0.3KFSI-0.5KPF$_6$ and 0.2KFSI-0.6KPF$_6$ electrolytes; (c) the corresponding mapping results of S and P for 0.3KFSI-0.5KPF$_6$ at 5.5 V. (d) S 2p and (e) P 2p XPS profiles by depth XPS analysis of the graphite cycled with 0.3KFSI-0.5KPF$_6$ and 0.2KFSI-0.6KPF$_6$.

To probe the chemical states and the possible interaction of the intercalants, XPS analysis was performed on the graphite powder that charged to 5.5 V under 0.3KFSI-0.5KPF$_6$ and 0.2KFSI-0.6KPF$_6$. We focus on the S 2p and P 2p spectra to compare the single and dual anion intercalation. The samples were etched using Ar ion beam for five minutes to avoid the interference from the surface S and P that existed in the CEI. As shown in Fig. 2d, the S 2p spectra show two separate peaks locating at 168.5 and 164 eV, respectively. While the former one results from the primary S=O species in FSI$^-$ anions with S possessing a valence of 6$^+$ [39],the other peak should correspond to the S-C species, where S bears a valence of 5$^+$ [40,41]. Compared with that in 0.3KFSI-0.5KPF$_6$, the S-C peak for 0.2KFSI-0.6KPF$_6$ is mildly weakened, suggesting that less FSI$^-$ is intercalated into the graphite. In terms of the status of PF$_6^-$, it first experiences hydrolysis upon dissolving, leading to the production of P-O$_x$F$_y$ species (134 eV), as confirmed in P 2p spectra (Fig. 2e) [42,43]. Apart from P-O$_x$F$_y$, the C-P species appear at 131.2 eV for both charged graphite samples [44]. Noticeably, the C-P signal of 0.2KFSI-0.6KPF$_6$ is overwhelmingly stronger than that of 0.3KFSI-0.5KPF$_6$, evidencing that more PF$_6^-$ is involved in the intercalation process. The results agree well with those obtained in EDS. More importantly, the only formation of S-C, C-P species indicates that although the intercalation of FSI$^-$ and PF$_6^-$ takes place concurrently, they react separately with graphite to form graphite intercalation compounds (GICs).

3.3 Real-time tracking of the intercalation

In-situ Raman scattering was then collected during the 1st and 2nd charge-discharge processes in 0.3KFSI-0.5KPF$_6$ and 0.7 M KPF$_6$ electrolytes to real-time monitor the intercalation process

(Fig. S9, S10). The intensity of the peaks in **Fig. 3**a is normalized to better present the spectra evolution. It indicates a highly reversible and similar pathway of the staging reactions for both electrolytes. To discuss in detail for 0.3KFSI-0.5KPF$_6$, one could observe that the initial G-Band at 1579 cm^{-1} splits into two separate peaks at early charging state. This stems from the presence of FSI$^-$/PF$_6^-$ in graphite layers, which causes frequency shift in the E$_{2g}$ mode of graphite in-plane vibration [9,45,46]. The peak located at 1581 cm^{-1} is referred to the graphite layers unattached to the intercalants, corresponding to an interior layer E$_{2g(i)}$ mode. The splitting peak at 1598 cm^{-1} represents the graphite layers adjacent to the intercalants and abides by a bounding layer E$_{2g(b)}$ mode. Aside from the successive shift in frequency, it shows a gradual loss of intensity for E$_{2g(i)}$ but a gain for E$_{2g(b)}$, implying more graphite layers are being intercalated by the anions. Based on the intensity ratio of E$_{2g(i)}$ (I_i) and E$_{2g(b)}$ (I_b), the intercalation stage (n>2) could be determined. As shown in equation (1) [47],
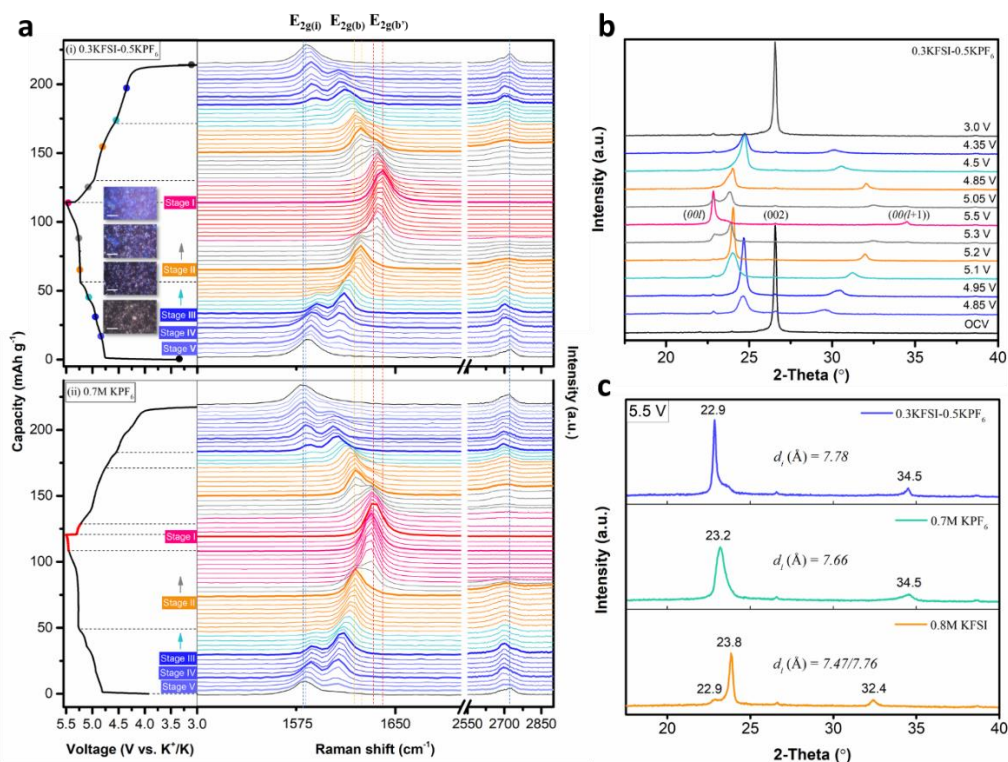
$$\frac{I_i}{I_b} = \frac{\sigma_i}{\sigma_b}\frac{(n-2)}{n} \tag{1}$$

Fig. 3. (a) *In*-situ Raman spectra and voltage profiles of FGF cathode using (i) 0.3KFSI-0.5KPF$_6$ and (ii) 0.7 M KPF$_6$ at 2nd cycle, insets of (i) show the real-time optical images of FGF cathode with a scale bar of 30 um; (b) *Ex*-situ XRD patterns of FGF electrodes at various states of charge/discharge corresponding to the colored dots in the charge-discharge curve for 0.3KFSI-0.5KPF$_6$; (c) *Ex*-situ XRD of FGF cathode charged to 5.5 V using different electrolytes.

the ratio σ_i/σ_b represents the Raman scattering cross-section, which could be approximately assumed to be 1. Accordingly, it indicates the formation of stage V (pale blue), stage IV (light blue) and stage III (dark blue) graphite-intercalation-compounds (GICs) at initial charging process. Upon further charging, the E$_{2g(b)}$ peak undergoes further blue shift from 1611 cm^{-1} of stage III GICs to 1615 cm^{-1}, along with the weakening and eventual disappear of E$_{2g(i)}$ peak (green colored). After this short transition, the Raman spectra exhibit a single E$_{2g(b)}$ peak indicating the formation of stage II GICs, by reason of the fact each graphite layer becomes adjacent to the intercalants. After charging to 5.2 V, the E$_{2g(b)}$ peak shifts to 1624 cm^{-1} at late stage II intercalation, followed by a distinct peak splitting (grey colored) with the emerging of another new peak E$_{2g2(b')}$. Soon after that, the original E$_{2g(b)}$ peak vanishes and the single-peak feature is regained for the Raman spectra. With the prominent E$_{2g(b')}$ peak (Fig. S9) and full disappearance of 2D-band, it suggests the formation of stage I GICs. For the discharge process, the Raman spectra demonstrate a reflective evolution path of the charge process. Particularly, the real-time optical images (inset) of the graphite were taken during the Raman experiment, indicating that low-stage (n≤2) GICs display a blue color.

The *in*-situ Raman spectra under 0.7 M KPF$_6$ are almost identical with that of 0.3KFSI-0.5KPF$_6$. For both electrolytes, the dilute-stage (n>3) intercalations occur before the long plateau region at around 5.25 V in the charge curves while the low-stage (n≤2) intercalations come about thereafter till 5.5 V. To correlate the staging reactions with the redox peaks of CV curves in Fig. 2a. It indicates that the O1, O2, O3, and O4 peaks should arise from the phase

transition of pristine/stage V (~4.78 V) → stage IV (~4.88 V), stage IV → stage III (~4.97 V), stage III → stage II (5.17-5.25 V), and stage II → stage I (5.27-5.39 V). It suggests the presence of dual anions does not alter the intercalation processes. The main difference between them comes from the degree of frequency shift upon intercalation. As denoted by the dashed sublines, the $E_{2g(b)}$ peak locates at 1624 cm^{-1} for 0.3KFSI-0.5KPF$_6$ and 1620 cm^{-1} for 0.7 M KPF$_6$ at late stage II. For stage I intercalation, the $E_{2g(b')}$ peak shows a continuous evolution from 1636 cm^{-1} to 1640 cm^{-1} at 5.5 V for 0.3FSI-0.5PF$_6$. By contrast, it remains almost fixed at 1632 cm^{-1} and undergoes an abrupt shift to 1634 cm^{-1} at the short plateau region (marked red) right below 5.5 V in the charge curve of 0.7M KPF$_6$, which is also well accorded with the O' peak at 5.45 V in its CV curve. The disparity of peak shift between two electrolytes may stem from the denser state of intercalants by FSI$^-$-PF$_6^-$ dual-ion intercalation, as indicated by its higher capacity [48]. In terms of the discharge process, the R1 redox peak corresponds to the phase transition of stage I → stage II (4.81/4.93 V for 0.3KFSI-0.5KPF$_6$/0.7 M KPF$_6$). R2 peak for 0.3KFSI-0.5KPF$_6$ covers the phase transition between stage II/stage III (~4.41 V) → stage IV (~4.39 V)/stage V (~4.30 V). Distinctively, for 0.7 M KPF$_6$, R1 redox is ascribed to the evolution of stage IV (~4.45 V) → stage V (~4.14 V) and R1' peak together with other trivial peaks (4.46-4.75 V) around it indicates the phase change of stage II → stage III (~ 4.53 V)/stage IV.

To further validate the staging mechanism, *ex*-situ XRD measurement was carried out on the FGF electrodes at various charge/discharge stages with 0.3KFSI-0.5KPF$_6$. As shown in Fig. 3b, the (002) plane of the pristine graphite splits into two dominant peaks upon charge, scilicet the one (00l) at 22.85°-24.65° and the other (00(l+1)) at 29.56°-34.49°. Based on the relation between the repeat distance along c-axis (I_c), intercalant gallery height (d_i) and the staging number (n), this series of XRD patterns evidence the following staging sequence (details are presented in Fig. S11 and Table S3): from pristine stage → stage IV (4.85 V) → stage III (4.95 V) → stage III/II (5.1 V) → stage II (5.2 V) → stage II/I (5.3 V) → stage I (5.5 V) during

charge and the same way back to pristine graphite upon discharge [49]. This is in good agreement with that retrieved by in-situ Raman, thus verifying the staging mechanism for FSI^--PF_6^- dual-ion intercalation.

Next, we focus on the analysis of the intercalation state for 0.8 M KFSI, 0.3KFSI-0.5KPF$_6$ and 0.7 M KPF$_6$ at 5.5 V via *ex*-situ XRD. As reflected in Fig. 3c, all of the XRD patterns indicate a stage I intercalation state except for that of 0.8 M KFSI, the status of which stands between stage II and stage I (calculation results shown in Table S4). It necessitates the incorporation of KPF$_6$ to improve the anionic stability for realizing a stage I state through charging to 5.5 V. The intercalant gallery height d_i shows a value of 7.76 Å and 7.66 Å for the stage I GICs formed in the electrolytes of 0.3KFSI-0.5KPF$_6$ and 0.7 M KPF$_6$. Apparently, FSI^--PF_6^- dual-anion intercalation leads to an increased d_i value due to the larger size of FSI^- 95 Å^3 (by van der Waal volume) than that of PF_6^- (69 Å^3) [48]. It again demonstrates the concurrent intercalation of FSI^- and PF_6^-.

3.4 Improved intercalation kinetics

One concern regarding the anion intercalation is the potential sluggish kinetics associated with the large intercalant radius. The rate capability of the cells using single and dual salt electrolytes are studied. As shown in **Fig. 4**a, with the 0.3KFSI-0.5KPF$_6$ electrolyte it delivers a discharge capacity of 100 mAh g^{-1} at 0.05 A g^{-1} with negligible capacity fading when the current density increased to 0.3 A g^{-1}. Under a high rate of 1.0 A g^{-1}, it remains 85% of the capacity at 0.05 A g^{-1}. Moreover, the capacity is almost recovered when the current density reduces back to 0.3 A g^{-1}. By contrast, with an increased ratio of KPF$_6$ in the dual-salt formula, as is the case of 0.2KFSI-0.6KPF$_6$, only 66% of the capacity at 0.05 A g^{-1} is retained at the rate of 1.0 A g^{-1}. Finally, it shows a poor rate capability for the single salt electrolyte, 0.7 M KPF$_6$. The capacity drops quickly from 97 mAh g^{-1} at 0.05 A g^{-1} to 36 mAh g^{-1} at 1.0 A g^{-1}. Besides, it bears a loss of approximately 10% reversible capacity after the current is recovered to 0.3 A

g^{-1}. The diffusivity of the electrolytes was then explored by CV rate scanning methods (Calculation details presented in Fig. S12). As shown in Fig. 4b, with the increase of the ratio of KPF$_6$, the average diffusion coefficients of the electrolytes exhibit a declining trend: 0.3KFSI-0.5KPF$_6$ > 0.2KFSI-0.6KPF$_6$ > 0.7 M KPF$_6$. This variation could come from the diffusivity difference between FSI$^-$ and PF$_6^-$ taking account of the fact that PF$_6^-$ plays a minor role in the intercalation process for 0.3KFSI-0.5KPF$_6$ electrolyte and should partly account for its better rate performance. In addition, the corresponding voltage profiles also suggest that the electrolyte of 0.7 M KPF$_6$ suffers from an intense polarization under large current density. Consequently, a deficient charge-discharge curve is seen for 0.2KFSI-0.6KPF$_6$ at 1.0 A g^{-1} (Fig. S13) and for 0.7 M KPF$_6$ at 0.5 A g^{-1} and higher rates (Fig. 4c), whereas an intact one could be retained for 0.3KFSI-0.5KPF$_6$ even at 1.0 A g^{-1} (Fig. 4d).
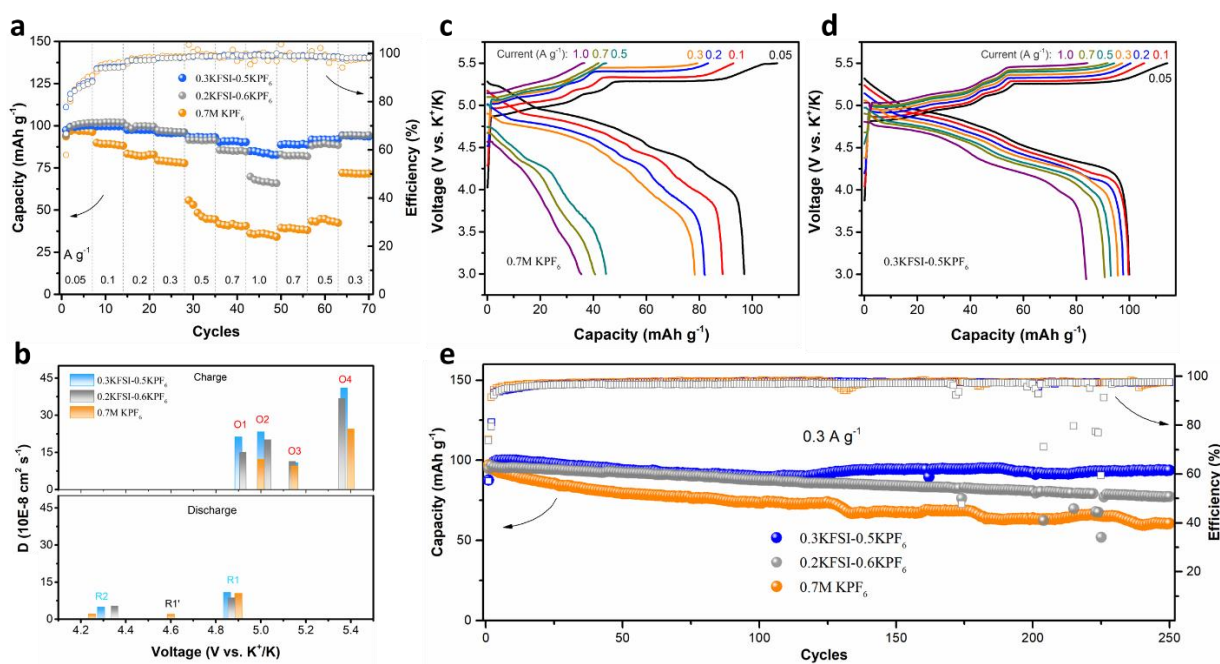

Fig. 4. (a) Rate test of 0.3KFSI-0.5KPF$_6$, 0.2KFSI-0.6KPF$_6$ and 0.7 M KPF$_6$ from 0.05 to 1.0 A g^{-1}. (b) Diffusion coefficient deduced by CV rate scanning method. The labels correspond to the peaks in Fig. 2a. Voltage profiles of (c) 0.3KFSI-0.5KPF$_6$ and (d) 0.7 M KPF$_6$ at different rates. (e) long-term cycling performance for 0.3KFSI-0.5KPF$_6$, 0.2KFSI-0.6KPF$_6$ and 0.7 M KPF$_6$ at the current rate of 0.3 A g^{-1}.

Lastly, the long-term cycling test is conducted for 0.3KFSI-0.5KPF$_6$, 0.2KFSI-0.6KPF$_6$ and 0.7 M KPF$_6$. As shown in Fig. 4e, a decent Coulombic efficiency of over 97% is obtained for all electrolytes except the first several cycles. The minor irreversibility is mainly due to the corrosion of current collectors at high potentials. For 0.3KFSI-0.5KPF$_6$, it delivers a capacity of 97.3 mAh g^{-1} and realizes a capacity retention of 96% after 250 cycles at 0.3 A g^{-1}. The obtained result is among the best of the state-of-the-art alkali-metal ion based dual ion systems, as shown in Table S5. By contrast, the capacity retention of the cell in 0.2KFSI-0.6KPF$_6$, where more PF$_6^-$ participates in the intercalation, drops to 80% over the same cycling period. Under 0.7 M KPF$_6$, the capacity decays from 94.9 to 60.7 mAh g^{-1} after 250 cycles, exhibiting a capacity retention of only 64%. It indicates that neat PF$_6^-$ intercalation may undermine the cyclic stability for PIBs at such a high potential. To testify this, the cycled FGF electrodes with 0.3KFSI-0.5KPF$_6$ and 0.7 M KPF$_6$ electrolytes are examined by Raman spectroscopy and XRD. Correspondingly, the Raman spectra of both samples and the pristine graphite have the G-band located at 1582 cm^{-1} (Fig. S14). However, the peak of the sample cycled in 0.7 M KPF$_6$ is broadened and shows a blue shift. Turning to the XRD result, it exhibits a characteristic sharp peak at 26.5° for pristine graphite and after cycling 0.3KFSI-0.5KPF$_6$ whilst a broadened peak at 25.8° is observed for that in 0.7 M KPF$_6$. Both the Raman and XRD tests indicate that the crystallinity of graphite remains intact under repeated co-intercalation/extraction of major FSI$^-$ and minor PF$_6^-$, while a structural deterioration is induced in the insertion of PF$_6^-$ alone. To examine the effect of K anodes on the cycling performance, the microstructure evolution of K anodes before and after cycling was characterized by AFM. The surface roughness of the K anode is prominently magnified after cycling in the above three electrolytes. As a illustration, the 3D surface topographies of K anode before and after cycling with 0.3KFSI-0.5KPF$_6$ are presented in Fig. S15. Micro-scale granular K particles are spotted on the cycled K anode as a result of potassium re-deposition, which is in good agreement with previous research [50]. Furthermore, symmetric K-K cells were tested with different electrolytes to investigate the K

anode behaviors. As shown in Fig. S16, short circuit occurs after 20~60 hours (equal to 20~60 cycles) for the K-K cells under large current, which is caused by the growth of granular K dendrite. The instability of K anode during repeatedly plating/stripping could lead to the microregional short circuit and causes unstable charge/discharge, as reflected by the fluctuation of efficiency for 0.2KFSI-0.6KPF$_6$ in Fig. 4e. We further examined the performance at a wide temperature range. Thanks to the improved kinetics and stable CEI, the binary KFSI-KPF$_6$ salt electrolyte outperforms the single salt counterpart at both 0 $^{\circ}$C and 45 $^{\circ}$C (Fig. S17).

4. Conclusions

Dual-anion intercalation strategy is utilized to boost the performance of P-DIBs. Compared to the widely adopted single-anion insertion, the approach in this work demonstrates significant advantages in realizing high-capacity and stable graphite-based cathode. The presence of KPF$_6$ helps achieve superior stability against oxidation at high potentials owing to the formation of an F-rich cathode electrolyte interface (CEI). Nevertheless, the single PF$_6^-$ insertion fails to deliver a long-term stability due to the structural deterioration upon repeated anion insertion/extraction. FSI$^-$ intercalation shows great advantages in the charge transfer kinetics together with exceptional stability. Concurrent intercalation of PF$_6^-$ and FSI$^-$ achieves a synergistic effect on the chemical stability and intercalation kinetics. Consequently, stage I GIC is formed, resulting in a reversible capacity of around 100 mAh g^{-1} with an average potential of 4.65 V (vs. K$^+$/K). The cell presents a capacity retention of 96% after 250 cycles at 0.3 A g^{-1}. The dual-anion intercalation approach provides new insights into the rational electrolyte design for of P-DIBs. In terms of practical implementation, future optimization should combine the dual-anion insertion approach and the high-concentration strategy for achieving a superior energy density in cell-level [19,51].

References

[1]   D. Larcher, J.M. Tarascon, Towards greener and more sustainable batteries for electrical energy storage, Nat. Chem. 7 (2015) 19–29.

[2]   H. Tan, X. Lin, J. Huang, J. Huang, M. Shi, X. Du, B. Zhang, The underestimated charge storage capability of carbon cathodes for advanced alkali metal-ion capacitors, Nanoscale. 11 (2019) 11445–11450.

[3]   M. Wang, Y. Tang, A Review on the Features and Progress of Dual-Ion Batteries, Adv. Energy Mater. 8 (2018) 1–20.

[4]   I.A. Rodríguez-Pérez, X. Ji, Anion Hosting Cathodes in Dual-Ion Batteries, ACS Energy Lett. 2 (2017) 1762–1770.

[5]   J. Zhu, Y. Li, B. Yang, L. Liu, J. Li, X. Yan, D. He, A Dual Carbon-Based Potassium Dual Ion Battery with Robust Comprehensive Performance, Small. 14 (2018) 1–6.

[6]   X. Jiang, X. Liu, Z. Zeng, L. Xiao, X. Ai, H. Yang, Y. Cao, A Nonflammable Na^+-Based Dual-Carbon Battery with Low-Cost, High Voltage, and Long Cycle Life, Adv. Energy Mater. 8 (2018) 1–9.

[7]   L. Fan, Q. Liu, S. Chen, Z. Xu, B. Lu, Soft Carbon as Anode for High-Performance Sodium-Based Dual Ion Full Battery, Adv. Energy Mater. 7 (2017) 1–8.

[8]   X. Zhang, Y. Tang, F. Zhang, C.S. Lee, A Novel Aluminum–Graphite Dual-Ion Battery, Adv. Energy Mater. 6 (2016) 1–6.

[9]   M. Angell, C.J. Pan, Y. Rong, C. Yuan, M.C. Lin, B.J. Hwang, H. Dai, High Coulombic efficiency aluminum-ion battery using an $AlCl_3$-urea ionic liquid analog electrolyte, Proc. Natl. Acad. Sci. U. S. A. 114 (2017) 834–839.

[10]   G. Wang, B. Kohn, U. Scheler, F. Wang, S. Oswald, M. Löffler, D. Tan, P. Zhang, J. Zhang, X. Feng, A High-Voltage, Dendrite-Free, and Durable Zn–Graphite Battery, Adv. Mater. 32 (2020).

[11]   L. Fan, Q. Liu, S. Chen, K. Lin, Z. Xu, B. Lu, Potassium-Based Dual Ion Battery with Dual-Graphite Electrode, Small. 13 (2017) 1–7.

[12]   B. Ji, F. Zhang, N. Wu, Y. Tang, A Dual-Carbon Battery Based on Potassium-Ion Electrolyte, Adv. Energy Mater. 7 (2017) 1–6.

[13]   B. Ji, F. Zhang, X. Song, Y. Tang, A Novel Potassium-Ion-Based Dual-Ion Battery, Adv. Mater. 29 (2017).

[14]   X. Han, G. Xu, Z. Zhang, X. Du, P. Han, X. Zhou, G. Cui, L. Chen, An In Situ Interface Reinforcement Strategy Achieving Long Cycle Performance of Dual-Ion Batteries, Adv. Energy Mater. 9 (2019) 25–28.

[15]   T. Ishihara, M. Koga, H. Matsumoto, M. Yoshio, Electrochemical intercalation of hexafluorophosphate anion into various carbons for cathode of dual-carbon rechargeable battery, Electrochem. Solid-State Lett. 10 (2007) 74–77.

[16]   S. Miyoshi, H. Nagano, T. Fukuda, T. Kurihara, M. Watanabe, S. Ida, T. Ishihara, Dual-Carbon Battery Using High Concentration $LiPF_6$ in Dimethyl Carbonate (DMC) Electrolyte , J. Electrochem. Soc. 163 (2016) A1206–A1213.

[17]   Q. Pan, D. Gong, Y. Tang, Recent progress and perspective on electrolytes for sodium/potassium-based devices, Energy Storage Mater. 31 (2020) 328–343.

[18]   K. Beltrop, S. Beuker, A. Heckmann, M. Winter, T. Placke, Alternative electrochemical energy storage: Potassium-based dual-graphite batteries, Energy Environ. Sci. 10 (2017) 2090–2094.

[19]   K. V. Kravchyk, P. Bhauriyal, L. Piveteau, C.P. Guntlin, B. Pathak, M. V. Kovalenko, High-energy-density dual-ion battery for stationary storage of electricity using concentrated potassium fluorosulfonylimide, Nat. Commun. 9 (2018).

[20]   X. Wang, F. Wang, L. Wang, M. Li, Y. Wang, B. Chen, Y. Zhu, L. Fu, L. Zha, L. Zhang, Y. Wu, W. Huang, An Aqueous Rechargeable $Zn//Co_3O_4$ Battery with High Energy Density and Good Cycling Behavior, Adv. Mater. 28 (2016) 4904–4911.

[21]   J. Zheng, M.H. Engelhard, D. Mei, S. Jiao, B.J. Polzin, J.G. Zhang, W. Xu, Electrolyte additive enabled fast charging and stable cycling lithium metal batteries, Nat. Energy. 2 (2017).

[22]   S. Jiao, X. Ren, R. Cao, M.H. Engelhard, Y. Liu, D. Hu, D. Mei, J. Zheng, W. Zhao, Q. Li, N. Liu, B.D. Adams, C. Ma, J. Liu, J.G. Zhang, W. Xu, Stable cycling of high-voltage

lithium metal batteries in ether electrolytes, Nat. Energy. 3 (2018) 739–746.

[23] B. Wen, Z. Deng, P.C. Tsai, Z.W. Lebens-Higgins, L.F.J. Piper, S.P. Ong, Y.M. Chiang, Ultrafast ion transport at a cathode–electrolyte interface and its strong dependence on salt solvation, Nat. Energy. 5 (2020) 578–586.

[24] Q. Liu, H. Wang, C. Jiang, Y. Tang, Multi-ion strategies towards emerging rechargeable batteries with high performance, Energy Storage Mater. 23 (2019) 566–586.

[25] X. Wu, Z. Xing, Y. Hu, Y. Zhang, Y. Sun, Z. Ju, J. Liu, Q. Zhuang, Effects of functional binders on electrochemical performance of graphite anode in potassium-ion batteries, Ionics (Kiel). 25 (2019) 2563–2574.

[26] J. Xu, S.L. Chou, Q.F. Gu, H.K. Liu, S.X. Dou, The effect of different binders on electrochemical properties of $LiNi_{1/3}Mn_{1/3}Co_{1/3}O_2$ cathode material in lithium ion batteries, J. Power Sources. 225 (2013) 172–178.

[27] N.S. Choi, Y.G. Lee, J.K. Park, Effect of cathode binder on electrochemical properties of lithium rechargeable polymer batteries, J. Power Sources. 112 (2002) 61–66.

[28] D. Zhu, L. Zhang, Y. Huang, J. Li, H. Fan, H. Wang, Ethylmethyl Carbonate's Role in Hexafluorophosphate Storage in Graphite Electrodes, ACS Appl. Energy Mater. (2019).

[29] D. Zhu, Y. Huang, L. Zhang, H. Fan, H. Wang, PF_6^- Intercalation into Graphite Electrode from Gamma-butyrolactone/ethyl Methyl Carbonate , J. Electrochem. Soc. 167 (2020) 070513.

[30] D. Möncke, H. Eckert, Review on the structural analysis of fluoride-phosphate and fluoro-phosphate glasses, J. Non-Crystalline Solids X. 3 (2019) 100026.

[31] J.M. Tarascon, A.S. Gozdz, C. Schmutz, F. Shokoohi, P.C. Warren, Performance of Bellcore's plastic rechargeable Li-ion batteries, Solid State Ionics. 86–88 (1996) 49–54.

[32] E.P. Dillon, C.A. Crouse, A.R. Barron, Synthesis, characterization, and carbon dioxide adsorption of covalently attached polyethyleneimine-functionalized single-wall carbon nanotubes, ACS Nano. 2 (2008) 156–164.

[33] B.J. Lindberg, K. Hamrin, G. Johansson, U. Gelius, A. Fahlman, C. Nordling, K. Siegbahn, Molecular Spectroscopy by Means of Esca, Phys. Scr. 1 (1970) 286–298.

[34] M. Chtaib, E.M. Roberfroid, Y. Novis, J.J. Pireaux, R. Caudano, P. Lutgen, G. Feyder, Polymer surface reactivity enhancement by ultraviolet ArF laser irradiation: An x- ray photoelectron spectroscopy study of polytetrafluoroethylene and

polyethyleneterepthalate ultraviolet treated surfaces, J. Vac. Sci. Technol. A Vacuum, Surfaces, Film. 7 (1989) 3233–3237.

[35] B.R. Strohmeier, Evaluation of polymeric standard reference materials for monitoring the performance of X-ray photoelectron spectrometers, Appl. Surf. Sci. 47 (1991) 225–234.

[36] C. Sleigh, A.P. Pijpers, A. Jaspers, B. Coussens, R.J. Meier, On the determination of atomic charge via ESCA including application to organometallics, J. Electron Spectros. Relat. Phenomena. 77 (1996) 41–57.

[37] G. Beamson, D. Briggs, High resolution monochromated x-ray photoelectron spectroscopy of organic polymers: A comparison between solid state data for organic polymers and gas phase data for small molecules, Mol. Phys. 76 (1992) 919–936.

[38] X. Fan, L. Chen, O. Borodin, X. Ji, J. Chen, S. Hou, T. Deng, J. Zheng, C. Yang, S.C. Liou, K. Amine, K. Xu, C. Wang, Non-flammable electrolyte enables li-metal batteries with aggressive cathode chemistries, Nat. Nanotechnol. 13 (2018).

[39] M. Döring, E. Uhlig, B. Undeutsch, K. Gloe, P. Mühl, Sulfonamidsubstituierte Thionoliganden als Komplexbildner für Kupfer(II) und als Extraktionsmittel für die späten 3d- Metallionen, ZAAC - J. Inorg. Gen. Chem. 567 (1988) 153–160.

[40] X. Wang, T. Gao, F. Han, Z. Ma, Z. Zhang, J. Li, C. Wang, Stabilizing high sulfur loading Li–S batteries by chemisorption of polysulfide on three-dimensional current collector, Nano Energy. 30 (2016) 700–708.

[41] P.M. Shanthi, P.J. Hanumantha, K. Ramalinga, B. Gattu, M.K. Datta, P.N. Kumta, Sulfonic Acid Based Complex Framework Materials (CFM): Nanostructured Polysulfide Immobilization Systems for Rechargeable Lithium–Sulfur Battery, J. Electrochem. Soc. 166 (2019) A1827–A1835.

[42] C. Peebles, R. Sahore, J.A. Gilbert, J.C. Garcia, A. Tornheim, J. Bareño, H. Iddir, C. Liao, D.P. Abraham, Tris(trimethylsilyl) Phosphite (TMSPi) and Triethyl Phosphite (TEPi) as Electrolyte Additives for Lithium Ion Batteries: Mechanistic Insights into Differences during $LiNi_{0.5}Mn_{0.3}Co_{0.2}O_2$ -Graphite Full Cell Cycling , J. Electrochem. Soc. 164 (2017) A1579–A1586.

[43] A.M. Andersson, D.P. Abraham, R. Haasch, S. MacLaren, J. Liu, K. Amine, Surface Characterization of Electrodes from High Power Lithium-Ion Batteries, J. Electrochem.

Soc. 149 (2002) A1358.

[44] J. Liu, H. Liu, Y. Zhang, R. Li, G. Liang, M. Gauthier, X. Sun, Synthesis and characterization of phosphorus-nitrogen doped multiwalled carbon nanotubes, Carbon N. Y. 49 (2011) 5014–5021.

[45] M.S. Dresselhaus, G. Dresselhaus, P.C. Eklund, Lattice Vibrations in Graphite and Intercalation Compounds of Graphite, Materials Science and Engineering. 31 (1977): 141-152.

[46] P. Kwizera, M.S. Dresselhaus, G. Dresselhaus, Raman spectra and staging of intercalated graphite fibers, Carbon N. Y. 21 (1983) 121–129.

[47] M. Balabajew, H. Reinhardt, N. Bock, M. Duchardt, S. Kachel, N. Hampp, B. Roling, In-Situ Raman Study of the Intercalation of Bis(trifluoromethylsulfonyl)imid Ions into Graphite inside a Dual-Ion Cell, Electrochim. Acta. 211 (2016) 679–688.

[48] H.B. Han, S.S. Zhou, D.J. Zhang, S.W. Feng, L.F. Li, K. Liu, W.F. Feng, J. Nie, H. Li, X.J. Huang, M. Armand, Z. Bin Zhou, Lithium bis(fluorosulfonyl)imide (LiFSI) as conducting salt for nonaqueous liquid electrolytes for lithium-ion batteries: Physicochemical and electrochemical properties, J. Power Sources. 196 (2011) 3623–3632.

[49] F. Kang, Electrochemical Synthesis of Graphite Intercalation Compounds with Low- or Non- Sulfur Content, Mech. Eng. Ph.D. degree thesis (1997).

[50] J. Hu, H. Wang, S. Wang, Y. Lei, L. Qin, X. Li, D. Zhai, B. Li, F. Kang, Electrochemical deposition mechanism of sodium and potassium, Energy Storage Mater. 36 (2021) 91–98.

[51] X. Li, X. Ou, Y. Tang, 6.0 V High-Voltage and Concentrated Electrolyte toward High Energy Density K-Based Dual-Graphite Battery, Adv. Energy Mater. 10 (2020) 1–7.